Computers & Fluids 100 (2014) 79–94

Contents lists available at ScienceDirect

Computers & Fluids

journal homepage: www.elsevier.com/locate/compfluid

Clothes washing simulations

Deniz Tolga Akcabay *, David R. Dowling, William W. Schultz

Department of Mechanical Engineering, University of Michigan, Ann Arbor, MI 48109-2133, USA

ARTICLE INFO

Article history:
Received 16 October 2013
Received in revised form 7 March 2014
Accepted 3 May 2014
Available online 15 May 2014

Keywords:
Washing machine
Computational fluid dynamics
Large deformation plate theory
Fluid structure interaction
Textiles
Immersed boundary method

ABSTRACT

Better washing machine designs and operation could reduce energy and water usage and extend cloth life. Washing machine studies have been traditionally empirical, since laundering typically involves complex motion of many cloth pieces in an inhomogeneous (fluid, cloth, detergent, agitator) setting. This paper presents a physics-based model of fully-submerged clothes washing in two- and three-dimensions. Multiple cloth pieces are modeled as thin elastic plates with tensile, shear, bending, and torsional stiffness, while the wash fluid is modeled with the incompressible Navier–Stokes equations. The fluid–cloth interaction is modeled via an immersed boundary method, and complex two- and three-dimensional agitator geometries are simulated with a Cartesian domain-mapping technique. The simulations have relatively coarse resolution that does not resolve all length scales for typical washing machine operating conditions. Hence, the converged results shown here are for moderate Reynolds numbers (Re). The simulation results include cloth stresses, torque on the wash basket, and the motion and deformation of the submerged cloth pieces. Specifically, the 3-D results show that the cloth stresses increase and the torque exerted on the outer wash basket decreases with increasing Re. The simulations examine how cloth motions differ with Reynolds number and cloth loading. The results reveal that for an agitator-driven 3-D wash geometry at higher Re, cloth pieces near the agitator at the bottom of the wash basket are first pushed by centrifugal force towards the outer stationary walls of the wash basket, then rise towards the top surface where they return to the axis of rotation and then sink towards the agitator. The variation of the center of mass positions of the cloth pieces are shown to increase for higher Re operating conditions.

1. Introduction

Clothes washing machines (washers) are ubiquitous in the modern world. However the clothes washing process has largely escaped a detailed computational analysis because a physically-meaningful numerical description of the relevant phenomena has not been formulated. Detailed physical descriptions of wash processes should account for the coupled, unsteady, complex, and three-dimensional motions of the fluid and cloth mixture when driven by the complex and moving geometries of the agitator and wash basket. Numerical solution strategies must simultaneously be appropriate for three-dimensional motion of a fluid and nearly arbitrary deformation of the cloth. This study describes a clothes washing simulation developed from first principles that attains these goals.

Most numerical models use computational grids with discrete points for solving the fluid and solid dynamic equations separately. However, if the grids are designed to conform to the domain boundaries, then the unsteady cloth motion and a moving agitator or wash basket would require redesigning the grid at every time-step, a task that could dominate the computational effort. Hence, most existing washing machine studies are limited to testing and empiricism. The studies given in [1–4] model washing machines by idealizing clothes as a single fabric ball and then analyzing its motion; [1] has also modeled each possible stage of the ball's motion in a horizontal-axis wash basket. Such reduced-order methods are suitable for real-time control designs.

However, higher-fidelity simulations are needed to improve designs to meet ever-increasing demands for better resource utilization. The empiricism in the existing models used for machine development – such as in [1] – are likely insufficient for preliminary design. Thus, models, such as that presented here that better capture the fundamental cloth–water–agitator interactions of washing machine processes are needed. Note that there is a rich literature on modeling and simulating cloth motion without coupling to a high-fidelity fluid model [5–11]; these models are mainly developed for the computer graphics industry.

The capabilities, characteristics, and limitations of the simulations reported here are as follows

* Corresponding author. Tel.: +1 (734) 214 1603.
E-mail addresses: dakcabay@umich.edu (D.T. Akcabay), drd@umich.edu (D.R. Dowling), schultz@umich.edu (W.W. Schultz).

http://dx.doi.org/10.1016/j.compfluid.2014.05.005
0045-7930/

- The simulations allow nearly arbitrary deformation of submerged pieces of cloth in a container with a complicated time-dependent shape.
- The submerged cloth pieces are modeled as elastic impermeable thin plates that undergo large deformations [12]. In particular, cloth pieces have appropriately high extensional and in-plane-shear stiffnesses, and appropriately low bending and torsional stiffnesses.
- The fluid is considered to be incompressible and viscous. Thus, the Navier–Stokes equations are solved through the model given in [13]. The fluid has the density of water, but its viscosity is elevated to prevent numerical problems at the modest grid resolutions of the current simulations.
- The cloth and fluid dynamics are coupled using an Immersed Boundary (IB) method [14]. In particular, the local fluid and cloth velocities are equal based on the viscous no-slip condition combined with cloth impermeability. The IB method has been used for many problems involving single and multiple flexible solids in viscous fluid flow (e.g. [15–21]).
- The moving solid surfaces of the washing machine's basket and agitator are modeled through a Cartesian domain-mapping technique. This approach avoids generation of a new grid at each time-step.
- The air–water interface is approximated as a flat perfect-slip surface.
- The modest-grid-resolution results presented here do not simulate all the scales of unsteady and turbulent fluid motion at the Reynolds numbers of representative washing processes. Thus, the current results are for moderate Reynolds numbers. Since this simulation attempt is the first of its kind, the emphasis here is on model development rather than high-resolution results.

The fluid/flexible-structure interaction component of the simulation is validated in [15,22] for problems involving the flutter regimes of thin cantilever beams, the natural frequencies of elastic plates, and the motion of a flexible filament in a gravity-driven viscous flow. Additionally, the method for handling the irregular geometries on a Cartesian grid is validated in this text for the problems of circular-Couette flow and the flow over a circular cylinder.

The remainder of this paper is organized as follows. In Section 2, the coupled equations of motion for the cloth pieces and the wash fluid are given. Here, the mechanical coupling of cloth and fluid is simulated by adding local body forces and density to the Navier–Stokes (fluid) equations to represent the stresses and inertial loads the cloth applies to the fluid. Then, in Section 3, a domain-mapping technique is described for simulating complex unsteady washing machine geometries with a stationary Cartesian grid. Section 4 introduces the simulation output measures. This is followed by the presentation of the two- and then three-dimensional simulations in Sections 5 and 6, respectively, with an emphasis on cloth motions and the cloth stresses. Finally, Section 7 summarizes this effort and provides conclusions.

2. Physical and numerical models for the fluid–cloth mixture

The current simulations use an Immersed Boundary (IB) method [14,23], to couple the motions of the cloth and fluid. The fluid and cloth have the same local velocity **u** so there is no relative slip or penetration at the cloth/fluid interface, and the Navier–Stokes equations have external forcing **f** due to the cloth loading to describe the combined motion of the fluid/cloth mixture:

$$\rho(\mathbf{x},t)\left(\frac{\partial \mathbf{u}(\mathbf{x},t)}{\partial t}+\mathbf{u}(\mathbf{x},t)\cdot\nabla\mathbf{u}(\mathbf{x},t)\right)=-\nabla p(\mathbf{x},t)+\mu\nabla^2\mathbf{u}(\mathbf{x},t)+\mathbf{f}(\mathbf{x},t), \tag{1}$$

$$\nabla\cdot\mathbf{u}(\mathbf{x},t)=0, \tag{2}$$

$$\mathbf{f}(\mathbf{x},t)=\int \mathbf{F}(\boldsymbol{\eta},t)\delta^*(\mathbf{x}-\mathbf{X}(\boldsymbol{\eta},t))K d\boldsymbol{\eta}, \tag{3}$$

$$\rho(\mathbf{x},t)=\rho_f+\int \frac{1}{K}\rho_s q\delta^*(\mathbf{x}-\mathbf{X}(\boldsymbol{\eta},t))K d\boldsymbol{\eta}, \tag{4}$$

$$\mathbf{U}(\boldsymbol{\eta},t)=\int \mathbf{u}(\mathbf{x},t)\delta^*(\mathbf{x}-\mathbf{X}(\boldsymbol{\eta},t))d\mathbf{x}, \tag{5}$$

$$\frac{D\mathbf{X}(\boldsymbol{\eta},t)}{Dt}=\mathbf{U}(\boldsymbol{\eta},t). \tag{6}$$

Here, **x** is the vector of independent spatial variables that parameterize the fluid volume, t is time, p is pressure, μ is the dynamic fluid viscosity. The location of a point on the deformed cloth mid-plane is $\mathbf{X}(\boldsymbol{\eta}, t)$, as shown in Fig. 1, where $\boldsymbol{\eta}=(r, s)$ and $\boldsymbol{\eta}=(s)$ are two- and one-dimensional parameterizations on the cloth mid-plane, for the three- and two-dimensional simulations, respectively. The simulations use two different grids: a moving Lagrangian mesh for discretizing $\boldsymbol{\eta}$ on the cloth, and a stationary Cartesian grid for discretizing the fluid volume **x**. K is the Jacobian of the deformed cloth mid-plane, ρ is the combined fluid/cloth mixture density, ρ_f is the uniform fluid density, ρ_s is the undeformed cloth density, while q is the cloth thickness ($\rho_s q$ is the mass per unit area of the cloth). **F** in Eq. (3) is the divergence of the cloth stress-resultants, derived briefly (with K) in the Appendix A and in more detail in [22], for a thin plate undergoing large elastic deformations. We will only mention here that **F** is related to: (1) the local extension/contraction, (2) the normal curvature, (3) the geodesic torsion, and 4) the surface shear at any point $\mathbf{X}(\boldsymbol{\eta}, t)$ for a given piece of cloth. Cloth thickness effects are included in **F** by the large-deformation plate theory; however the cloth thickness is not geometrically modeled as the clothes are assumed to be 2-D elements embedded in a 3-D fluid volume. The external forcing **f** in Eq. (1) is related to **F** through the relation given in Eq. (3). For a 2-D piece of cloth in a 3-D fluid volume, **F** is a 2-D quantity – it is defined throughout the deformed cloth mid-plane $\boldsymbol{\eta}$ – and hence $\mathbf{F}=\mathbf{F}(\boldsymbol{\eta}, t)$, but note that Eq. (1) and **f** are defined for the 3-D fluid volume. Eq. (3) constructs **f** by using **F** and regularized Dirac delta function δ^*. The same approach is used for expressing the 2-D cloth density $\rho_s q$ in 3-D via Eq. (4). The function δ^* in Eqs. (3)–(5) is a smooth approximation to a three-dimensional Dirac delta function and is described in Eqs. (7) and (8) below.

Eq. (5) determines the cloth velocity **U** from the fluid velocity field **u,** while Eq. (6) defines the Lagrangian advection of the cloth pieces. On the undeformed cloth mid-plane, r and s are arclength parameters that are everywhere orthogonal. In Fig. 1, $\mathbf{e_s}$ and $\mathbf{e_r}$ are unit vectors tangent to constant r and s lines and $\mathbf{e_n}=\mathbf{e_s}\times\mathbf{e_r}/|\mathbf{e_s}\times\mathbf{e_r}|$ is the cloth-surface normal vector.

The cloth pieces are assumed to be thin, so cloth elastic and inertial forces are first multiplied with the uniform cloth thickness, and then these local forces are spread onto the fluid grid using a regularized Dirac delta function δ^*, as in Eqs. (3) and (4). As suggested in [23] for $\mathbf{x}\in\mathbf{R^3}$, δ^* is approximated with a Cartesian product of one-dimensional functions ϕ:

$$\delta^*(\mathbf{x})=\phi(x)\phi(y)\phi(z), \quad \text{where } \mathbf{x}=(x,y,z), \tag{7}$$

and

$$\phi(r)=\begin{cases}\frac{1}{2\varepsilon}\left(1+\cos\left(\frac{\pi r}{\varepsilon}\right)\right), & \text{if } |r|\leqslant\varepsilon\\ 0, & \text{otherwise}\end{cases}. \tag{8}$$

For $\mathbf{x}\in\mathbf{R}^2$ the approximation is similar, but in this case $\delta^*(\mathbf{x})=\phi(x)\phi(y)$. The one-dimensional regularized Dirac delta function ϕ has a compact support width of 2ε. In the simulations

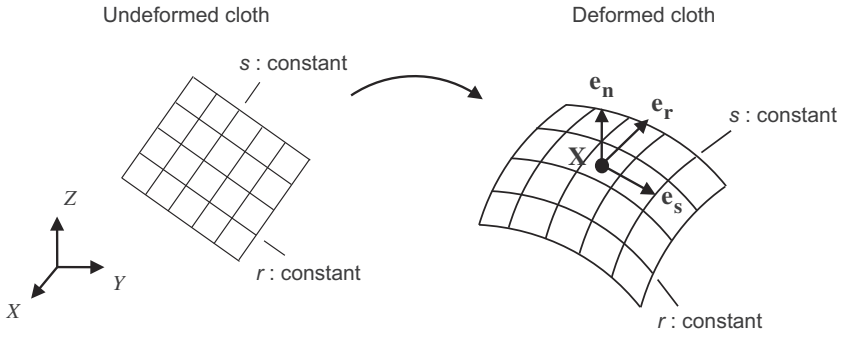

Fig. 1. Deformation of the mid-plane of a rectangular cloth piece.

presented next, for each component $\phi(x)$, $\phi(y)$, and $\phi(z)$, ε is chosen as $2h_x$, $2h_y$, and $2h_z$, respectively, where h_x, h_y, and h_z are the fluid grid spacings along the x, y, and z directions. In this form, the δ^* value on a fluid grid point $\mathbf{x_{i,j,k}}$ is nonzero only if it is near a cloth piece.

The Navier–Stokes Eqs. (1) and (2) are solved with a fractional step method described in [13]. The weak forms of the equations are discretized with second-order accurate interpolations and integrations, as the fluid volume is discretized with the finite-volume Cartesian grid Marker-and-Cell (MAC) method shown in [22]. Briefly, the simulations use the implicit Crank-Nicolson method for the viscous terms and the 3/2 Adams–Bashforth method for the convective terms in time; these time discretizations are given in detail in [22]. The simulations use a forward Euler method for the three-dimensional computations and the implicit Broyden method [24–26] for the two-dimensional computations for solving Eq. (6). The details of this process can be found in [22]. The physical and numerical models were verified in [15,22] as noted above.

3. Numerical method for unsteady flow in complex geometries

Vertical-axis washing machines stir the fluid–cloth mixture using a moving agitator with a complex three-dimensional geometry. Computations are more expedient using a non-conforming Cartesian grid (an example is Fig. A.1) to incorporate such irregular non-stationary domain boundaries rather than remeshing the fluid grid at every time step. This simulation achieves this by transforming Eqs. (1) and (2) to:

$$\left[\rho\left(\frac{\partial \mathbf{u}}{\partial t}+\mathbf{u}\cdot\nabla\mathbf{u}\right)+\nabla p-\mu\nabla^2\mathbf{u}-\mathbf{f}\right](1-H(\psi))+k_o[\mathbf{u}-\mathbf{u}_o]H(\psi)=0, \tag{9}$$

$$\nabla\cdot\mathbf{u}=0, \tag{10}$$

Eq. (9) results in $\mathbf{u}=\mathbf{u_o}$ when $H(\psi)=1$ and Eq. (1) when $H(\psi)=0$, where H is a regularized or sharp Heaviside function; a general regularized H is given as:

$$H(\psi)=\begin{cases}0 & \text{if } \psi<-\gamma\\ \frac{1}{2}+\frac{1}{2}\left(\frac{\psi}{\gamma}+\frac{1}{\pi}\sin\left(\frac{\pi\psi}{\gamma}\right)\right) & \text{if } |\psi|\leqslant\gamma\\ 1 & \text{if } \psi>\gamma\end{cases} \tag{11}$$

Alternatively, a sharp Heaviside function is also defined as $H(\psi)=0$ for $\psi<0$, $H(\psi)=1/2$ for $\psi=0$, and $H(\psi)=1$ for $\psi>0$. In Eq. (9), ψ is a prescribed scalar function that is negative in the fluid–cloth mixture and greater than zero elsewhere; $\mathbf{u_o}$ is the prescribed velocity field outside the fluid–cloth mixture. k_o in Eq. (9) is a scalar constant, which is selected in such a way that the diagonal terms in the resulting matrix equations are the same in both the fluid and solid regions. In Eq. (11), γ controls how the regularized Heaviside function is spread onto the fluid grid points – note that if using a sharp H, the value of k_o would not have any effect on the results. Appendix B includes a comparative analysis of the accuracy of the simulation for both a sharp and a regularized H-function. The numerical tests given in Appendix B show that the sharp implementation of $H(\psi)$ is more accurate than the smooth formulation for the test problems at least on grid sizes used here, so a sharp H-function is used in the simulations. A similar formulation has also been given in [27,28]. For example for an external flow over a cylinder of a radius R with center at (x_o, y_o): $\psi=-(x-x_o)^2-(y-y_o)^2+R^2$. For complex geometries, such as the 3-D agitator of a washing machine, ψ is found from making mathematical operations between elemental ψ functions for simple geometries; for example $\psi=\max(\psi_1,\psi_2)$, where $\psi_1=-(x-x_{o,1})^2-(y-y_{o,1})^2+R_1^2$ and $\psi_2=-(x-x_{o,2})^2-(y-y_{o,2})^2+R_2^2$ would be the augmented geometry of two overlapping circles if $(x_{o,1}, y_{o,1})$ and $(x_{o,2}, y_{o,2})$ are close. After generating ψ functions in this manner, they are transformed to distance functions [22]. Note that for moving but rigid solid objects (surrounding the fluid–cloth mixture, i.e. the washing machine walls and agitator) $\nabla\cdot\mathbf{u_o}=0$.

4. Characterization of the simulation outputs

If cloth is primarily cleaned by the relative motion of cloth pieces, one of the most valuable simulation predictions would be cloth motion under different specified agitations. Additionally, the statistics of cloth stresses help predict cloth wear and cloth life. At any point $\mathbf{X}$ on the deformed mid-plane of a given cloth piece with a uniform thickness q, the large deformation plate theory gives that the largest extensional strains occur at a distance $q/2$ away normal to the mid-plane. So the maximum cloth strains could be expressed as:

$$\begin{aligned}|e_{ss}|_{max}&=\left|\frac{1}{2}\left(1-1\Big/\left|\frac{\partial\mathbf{X}}{\partial s}\right|^2\right)\right|+\left|\frac{q}{2}\kappa_s\right|,\\ |e_{rr}|_{max}&=\left|\frac{1}{2}\left(1-1\Big/\left|\frac{\partial\mathbf{X}}{\partial r}\right|^2\right)\right|+\left|\frac{q}{2}\kappa_r\right|,\\ |e_{sr}|_{max}&=\left|\frac{1}{2}\left(\frac{\partial\mathbf{X}}{\partial s}\cdot\frac{\partial\mathbf{X}}{\partial r}\right)\Big/\left|\frac{\partial\mathbf{X}}{\partial s}\right|\left|\frac{\partial\mathbf{X}}{\partial r}\right|\right|+\left|\frac{q}{2}\left(\frac{\partial^2\mathbf{X}}{\partial s\partial r}\cdot\mathbf{e}_n\right)\Big/\left|\frac{\partial\mathbf{X}}{\partial s}\right|\left|\frac{\partial\mathbf{X}}{\partial r}\right|\right|,\end{aligned} \tag{12}$$

where κ_s and κ_r are the normal curvatures of the constant r and s lines (derived in Appendix A), respectively, in Fig. 1. Next, linear and isotropic plane stress–strain relations are used to estimate the maximum cloth stress magnitudes as:

$$\begin{pmatrix}|\sigma_{ss}|_{max}\\ |\sigma_{rr}|_{max}\\ |\sigma_{sr}|_{max}\end{pmatrix}=\frac{E}{1-\nu^2}\begin{pmatrix}1 & \nu & 0\\ \nu & 1 & 0\\ 0 & 0 & 1-\nu\end{pmatrix}\begin{pmatrix}|e_{ss}|_{max}\\ |e_{rr}|_{max}\\ |e_{sr}|_{max}\end{pmatrix} \tag{13}$$

where E is the cloth Young's modulus and v is Poisson's ratio. Note that the points with the highest bending stresses are the same points where the maximum von Mises stresses $|\bar{S}_{vM}|_{max}$ occur. In the 3-D results presented in Section 6, only the von Mises stress equivalents of all the three stress components shown in Eq. (13) will be presented – note that for the 2-D fluid simulations with 1-D cloth pieces there is only one stress component for the cloth. Following Eq. (13) and Appendix A, the next sections use the following stiffness constants:

$$K_e \equiv \frac{Eq}{1-v^2}, \quad K_s \equiv \frac{Eq}{1+v}, \quad K_b \equiv \frac{Eq^3}{12(1-v^2)}, \quad K_t \equiv \frac{Eq^3}{12(1+v)} \tag{14}$$

which are, respectively, extensional, in-plane shear, bending, and torsional cloth stiffness for a cloth piece with a uniform thickness q.

Aref [29] showed that the advection of particles even in laminar flows would become chaotic if the velocity field is unsteady. Chaotic systems may have different results for slightly different conditions, including different simulation time-step and mesh size [30]. However, their statistics are better behaved. For this reason, the present simulation results report average absolute maximum cloth stresses of all cloth pieces, as:

$$\overline{|\sigma|}_{max} = \frac{1}{N_{\text{cloth}}} \sum_{k=1}^{N_{\text{cloth}}} \frac{1}{A_k} \int \overline{|\sigma|}^{k}_{max} dA_k, \tag{15}$$

where N_{cloth} is the total number of cloth pieces, A_k is the surface area of each cloth piece, and $\overline{|\sigma|^k_{max}}$ is the time average of the absolute maximum cloth stress σ_{ij} through Eq. (13) for each cloth computational point. This time averaging is done over a few washing machine cycles (specifically noted for each result) after cropping the initial transient effects. The simulations also report the standard deviations of the cloth stresses during the same time periods.

5. Two-dimensional simulations

The two-dimensional washing machine simulations presented here are developmental, since they cannot capture the vertical tumbling motion of the cloth pieces in a vertical-axis washing machine. Plus, the simulations assume a fully-wetted wash basket without the dynamic free-surface present in horizontal-axis machines. However, they help to verify and illustrate the simulation development.

5.1. Washtub and the initial cloth placements

The simulation setup is as given in Fig. 2. The wash geometry consists of an outer stationary circular wall (basket) and a rotating agitator. Fig. 2 also shows the initial placement of twenty cloth pieces in the 2D simulations. In all these simulations the washtub geometry and the initial cloth placements are not varied. The cloth pieces are randomly placed without overlap, and these cloth pieces have two different lengths and different (constant) curvatures.

5.2. Operating conditions, physical parameters, and other numerical simulation details

Unless noted otherwise, the operating conditions and the various physical and numerical properties are as given in Table 1, where h is the uniform mesh-size of the Cartesian grid for solving Eqs. (9) and (10). The exact values of h are given later in the results section. The Lagrangian mesh size mentioned in Table 1 is for flat unstretched cloth. The average Lagrangian to Eulerian mesh size ratio was selected as unity, because it was shown in [22] that these simulations are prone to numerical instabilities with ratios less than 1. The angular speed of the agitator is prescribed by

$$\omega = \omega_{max} \sin(2\pi f t), \tag{16}$$

where f is the agitator frequency. The outer wall is stationary. Hence, $\mathbf{u}_o$ in Eq. (9) is constructed such that $\mathbf{u_o} = \omega \mathbf{e_Z} \times \mathbf{r}$ inside the agitator, where $\mathbf{e_Z}$ is the unit vector along the Z-axis, and $\mathbf{u_o} = \mathbf{0}$ outside the wash tub. In Table 1 the cloth excess mass density is with respect to water and is zero if the cloth is neutrally buoyant in water.

Note that the fluid viscosity here is 1000 times that of water to lower the computational requirements during simulation development.

5.3. Dimensionless groups

The following length, time, and mass scales in these simulations

$$l^o = r_o, \quad t^o = 1/\omega_{max}, \quad M^o = \rho_f r_o^3, \tag{17}$$

lead to the dimensionless parameters:

$$\text{Re} = \frac{\rho_f r_o^2 \omega_{max}}{\mu}, \quad \text{Te} = \frac{K_e}{\rho_f \omega_{max}^2 r_o^3}, \quad \text{Be} = \frac{K_b}{\rho_f \omega_{max}^2 r_o^5}, \quad \text{In} = \frac{\rho_s q}{\rho_f r_o}, \quad \text{St} = \frac{f}{\omega_{max}}. \tag{18}$$

In Eq. (18), Re is the Reynolds number, Te is the ratio of the cloth extensional stiffness force to fluid inertial force, Be is the ratio of the cloth bending stiffness force to the fluid inertial force, In is the ratio of the cloth to fluid inertia, and St is the Strouhal number (dimensionless frequency). The dimensional values given in Table 1 and Fig. 2 correspond to the following dimensionless values in all the two-dimensional simulations unless noted otherwise:

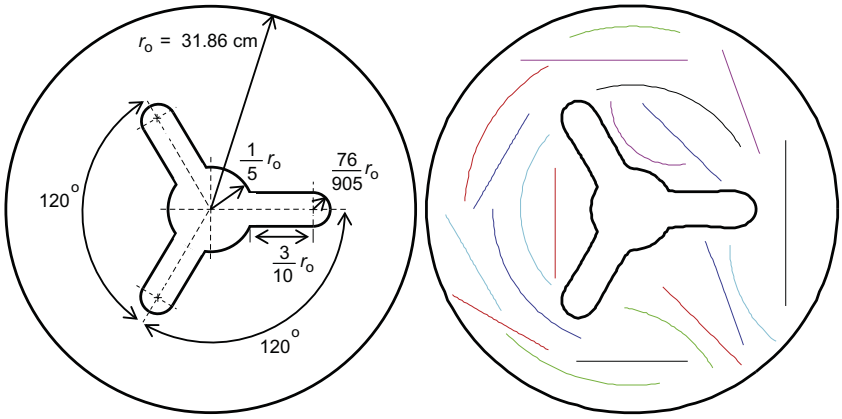

Fig. 2. The washtub geometry for the two-dimensional simulations and the initial placements of the twenty cloth pieces.

Table 1
Operating conditions, physical and numerical parameters in the 2D simulations.

Radius of the other basket (r_o)	31.86 cm
Mesh size (h/r_o)	33.9×10^{-3}–4.2×10^{-3}
Agitator's peak rotation speed (ω_{max})[a]	120 rpm
Agitator rotation frequency (f)[a]	$2/\pi$ Hz
Cloth extensional stiffness (K_e)	8×10^3 N/m
Cloth bending stiffness (K_b)	1×10^{-5} N.m
Cloth excess mass density ($\rho_s q$)[b]	9.3×10^{-2} kg/m^2
Length of the cloth pieces	26.08 & 17.39 cm
Average cloth thickness (q)	2.4×10^{-4} m
Fluid density (ρ_f)	1000 kg/m^3
Fluid dynamic viscosity (μ)	1 kg/(m s)
Number of cloth pieces	20
Dirac delta function half width (ε)	$2h$
Average Lagrangian to Eulerian mesh size ratio	1

[a] The agitator makes one full revolution before reversing.
[b] Relative to a neutrally-buoyant cloth piece in water (=0 if neutrally buoyant).

$$\mathrm{Re} = 1300, \quad \mathrm{Te} = 1.6, \quad \mathrm{Be} = 1.9 \times 10^{-8}, \quad \mathrm{In} = 2.9 \times 10^{-4}, \quad \text{and } \mathrm{St} = 0.05.$$

5.4. Results

The simulations predicted significantly different cloth trajectories with successively refined time-step and mesh-size, in agreement with the observations of chaotic advection of particle paths in unsteady flows [29]. However, the statistics of the average absolute cloth stress and the root mean square value of the torque on the outer wall were observed to converge acceptably. Specifically, Table 2 shows the effect of changing the uniform dimensionless Eulerian mesh size h/r_o on the statistics of the absolute cloth stresses scaled by $\sigma_o = \rho_f r_o^2 \omega_{max}^2$ and on the dimensionless 2-D rms torque exerted on the outer washtub cylinder scaled by $\tau_o = \rho_f r_o^4 \omega_{max}^2$. These simulations were conducted with the dimensionless time-step $\Delta t \omega_{max} = 9.42 \times 10^{-5}$. The (dimensionless) value $h/r_o = 4.2 \times 10^{-3}$ corresponds to an Eulerian grid size of 513×513 points, and the simulation video is attached as a supplemental file to this paper.

The stresses in Table 2 are larger using poorer resolution due to the unresolved complex cloth wrinkles. It has been shown in Ref. [22] that a minimum Lagrangian to Eulerian grid size ratio about unity is required to ensure accurate and stable results using the current fluid–structure-interaction coupling method (the immersed boundary method), so it is not useful to increase the Lagrangian points on the cloth without simultaneously refining the Eulerian grid. Table 2 also shows that the dimensionless rms torque estimate on the outer wall is within 7% for the finest two grids. Additionally, Table 3 confirms the relative insensitivity of changing the time-step for $h/r_o = 17.0 \times 10^{-3}$.

The simulations showed that the cloth pieces preserve their initial length as they move and deform in the 2-D washtub; their motion was observed to be fast near the tip of the agitator as they get wrinkled. Note that, since the present 2-D fluid, 1-D cloth simulations are only developmental, more results will be analyzed in Section 6 for the motion of 2-D cloth pieces in 3-D fluid. As a sample illustration, the effect on cloth motion of changing cloth bending stiffness is shown in Fig. 3 with Re = 1300, $h/r_o = 17.0 \times 10^{-3}$ and $\Delta t \omega_{max} = 1.9 \times 10^{-4}$. The vertical sequence of snapshots in the left column of Fig. 3 shows the motion of a thicker (or stiffer) cloth with $\mathrm{Be} = 1.9 \times 10^{-5}$. The time duration between each frame is approximately a quarter period of the agitator rotation cycle, so the agitator rotates about 180° between each snapshot. Fig. 3 shows that the cloth pieces with smaller Be wrinkle more, which is expected based on a prior analysis of flexible filaments in fluid flow [18].

Table 2
The effect of Eulerian mesh refinement on the statistics of the absolute cloth stresses and the rms torque on the outer wall between the beginning of the second and the fourth agitation cycles, as the agitator completes 4 full revolutions in opposite directions. These simulations use Re = 1300 and $\Delta t \omega_{max} = 9.42 \times 10^{-5}$.

h/r_o	$\lvert\bar{\sigma}\rvert_{max}/\sigma_o$	Standard deviation in σ	(rms torque on the outer wall)/τ_o
33.9×10^{-3}	24.0	10.3	Not measured
17.0×10^{-3}	9.4	3.2	4.0×10^{-3}
8.5×10^{-3}	5.6	1.0	1.4×10^{-3}
4.2×10^{-3}	4.9	0.9	1.5×10^{-3}

6. Three-dimensional simulations

Unlike the 2-D case, 3-D simulations can predict the axial tumbling motion of cloth pieces in a vertical-axis washing machine. However, the computational cost of these simulations is higher, and, since the emphasis here is on model development, the coarse grid results presented here represent moderate Re operating conditions.

There are many ways the flow can become three-dimensional. The agitator may have a three-dimensional shape or it may have finite axial extent. Even if the agitator is two-dimensional, instabilities lead to periodic role cells similar to that seen in Taylor-Couette flow or the finite extent of the cloth in the axial (vertical) direction would force 3-D behavior. Complicated free-surface or tub-bottom conditions would make the problem 3-D, as would the common practice of axial agitator motion. For the case studied here, three-dimensional motion is primarily caused by the agitator shape, and the finite extent of the agitator and cloth pieces in the axial (vertical) direction.

6.1. Washtub geometry and initial cloth positions

This study pertains to a vertical-axis washing machine. Figs. 4 and 5 illustrate the threefold-symmetric washing machine agitator. In Fig. 4, z is the wash basket's vertical axis and is zero at the flat basket bottom, while x' and y' are body-attached orthogonal axes that span the horizontal plane defining one-third of the threefold symmetric agitator, with their origin at the axis of rotation of the agitator. In addition to the moving agitator, the washtub is assumed to have an outer stationary cylinder with a radius of 31 cm. Fig. 5 is an image of the appearance of the washtub geometry using the level-set function ψ described in Section 3 with a Cartesian grid resolution of $33 \times 33 \times 33$ points. In the following simulations the grid resolution varies from $33 \times 33 \times 33$ to $65 \times 65 \times 65$ points. Fig. 5 also shows the air–water interface, modeled as a perfect-slip flat surface, at a height $H = 23.76$ cm above the washtub bottom.

All simulations shown here have square (15 cm × 15 cm) cloth pieces, initially positioned in a radial arrangement with small individual shifts and tilts to obtain a random cloth configuration quickly. In the simulations shown next, each cloth piece is discretized with 7×7 to 14×14 Lagrangian grid points.

6.2. Operating conditions, physical parameters, and other numerical simulation details

Table 4 lists the operating conditions, and physical and numerical parameters in these simulations, unless noted otherwise. In Table 4, h_{vertical} is the Eulerian mesh size along the vertical z-direction, while h_{lateral} is the Eulerian mesh size along the lateral (x, y) axes (note that as explained in Section 3, the simulation uses

Table 3
Effect of changing the time step on the statistics of the absolute cloth stresses between the beginning of the second and third agitation cycles, with Re = 1300, $h/r_o = 17.0 \times 10^{-3}$.

$\Delta t\omega_{max}$	$\overline{\lvert\sigma\rvert}_{max}/\sigma_o$	Standard deviation
1.9×10^{-4}	8.9	2.6
$1.9 \times 10^{-4}/2$	8.3	2.5
$1.9 \times 10^{-4}/4$	8.9	2.6

a Cartesian mesh to model the washing machine geometry). Also, the Lagrangian mesh size in Table 4 is measured along the constant *r*- and *s*-lines on the cloth pieces that are defined in Section 2. The computational domain is three times wider in its lateral directions than its height, and the simulation uses a three times denser Cartesian grid along the vertical axis. Note that in Table 4 the dynamic viscosity of the fluid is mentioned to vary between 10^{-1} and 10^{1} [kg/(m s)], which corresponds to a Re between 12,000 and 120. The agitator angular speed is given through Eq. (16), and the outer wall is stationary. Hence, $\mathbf{u}_o$ in Eq. (9) is constructed such that $\mathbf{u_o} = \omega \mathbf{e_Z} \times \mathbf{r}$ inside the agitator, where $\mathbf{e_Z}$ is the unit vector along the Z-axis, and $\mathbf{u_o} = \mathbf{0}$ outside the wash tub. Note that the simulations were observed in [22] to be prone to numerical instabilities with Lagrangian to Eulerian ratios less than unity, so a higher than 1 ratio is selected.

6.3. Dimensionless groups

The dimensionless groups are similar to the ones given for the 2-D simulations. The length, time, and mass scales are the same. In addition to Eq. (18), the following additional dimensionless groups are introduced:

$$\mathrm{Se} = \frac{K_s}{\rho_f \omega_{max}^2 r_o^3}, \quad \mathrm{To} = \frac{K_t}{\rho_f \omega_{max}^2 r_o^5}. \tag{19}$$

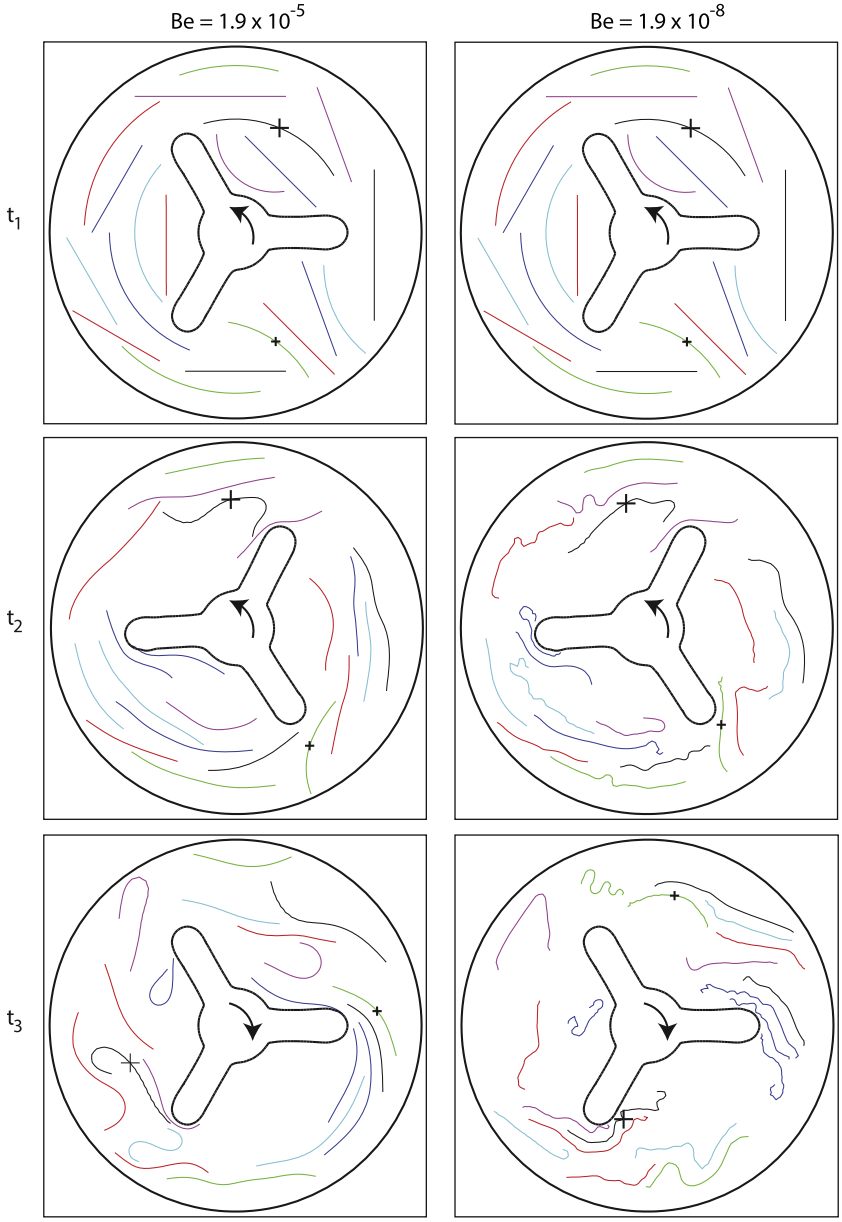

Fig. 3. The effect of changing bending stiffness on cloth motion in 2-D with Re = 1300, $h/r_o = 17.0 \times 10^{-3}$ and $\Delta t\omega_{max} = 1.9 \times 10^{-4}$. The snapshots in the left column are for Be = 1.9×10^{-5} and the snapshots in the right column are for Be = 1.9×10^{-8}. Snapshots differ by a quarter period of the agitator cycle corresponding to a 180° rotation. Markers+ are attached on two different clothes to aid tracing.

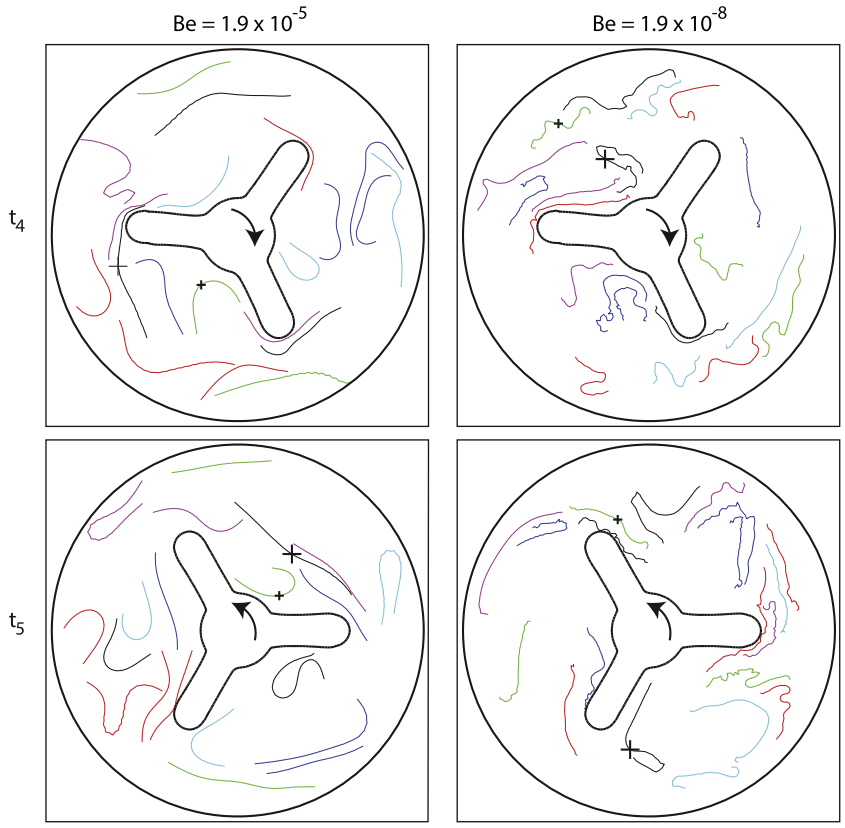

Fig. 3 (*continued*)

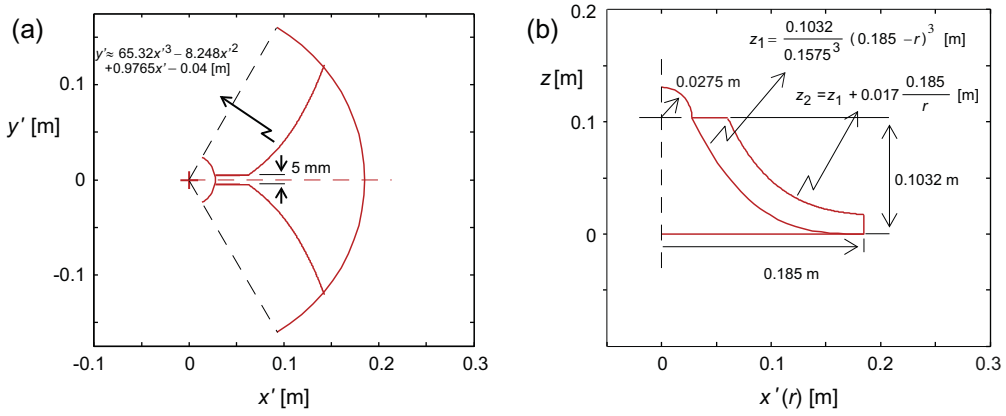

Fig. 4. A partial simplified view of the agitator. The left plot is the top view and the right plot is the front view of the mid-section of the 1/3th symmetric part of the agitator.

In Eq. (19), Se and To are the ratios of the cloth in-plane shear and torsional stiffness forces to fluid inertial forces. The dimensional values given in Sections 6.1 and 6.2 yield the following dimensionless values in the simulations unless noted otherwise.

$$\mathrm{Re} = 12{,}000 \text{ to } 120, \quad \mathrm{Te} = 170, \quad \mathrm{Se} = 6.4 \times 10^{-2},$$

$$\mathrm{Be} = 2.2 \times 10^{-8}, \quad \mathrm{To} = 2.2 \times 10^{-8}, \quad \mathrm{In} = 3.0 \times 10^{-4}, \quad \mathrm{St} = 0.05.$$

6.4. Results

The effect of changing the grid resolution is examined for 16 cloth pieces for Re = 1200 and 120, where Re for a typical wash cycle is of order 10^6. The computational cost of the three-dimensional simulations prevented finer resolution simulations for higher Re. Table 5 shows the effect of changing the dimensionless lateral Eulerian mesh size h_{lateral}/r_o on the absolute von Mises Lagrangian stresses $|\bar{S}_{vM}|_{max}$ scaled by $\sigma_o = \rho_f r_o^2 \omega_{max}^2$ (the $h_{\text{lateral}}/h_{\text{vertical}}$ ratio is fixed). Table 6 shows the effect of h_{lateral}/r_o on the rms torque exerted on the outer cylinder, scaled by $\tau_o = \rho_f r_o^4 \omega_{max}^2 H$. These simulations use dimensionless time-step $\Delta t \omega_{max} = 5.0 \times 10^{-4}$, and the statistics were measured between the fourth and the twelfth agitation cycles. The Lagrangian to Eulerian mesh width ratio was kept constant near 1 and the value $h_{\text{lateral}} = 3.5 \times 10^{-2}$ corresponds to an Eulerian grid size of $65 \times 65 \times 65$ points.

Table 5 shows that for Re = 120 the dimensionless cloth stresses fluctuate between 6 and 7; for Re = 1200 the stresses decrease as the grid is refined, but the 33% decrease between $h/r_o = 7 \times 10^{-2}$

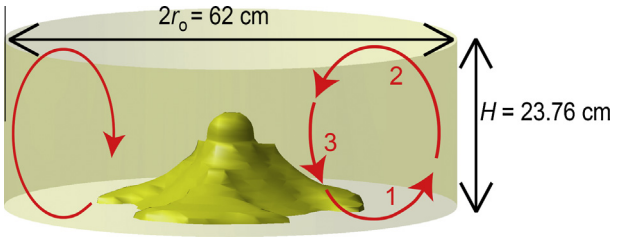

Fig. 5. The washtub geometry as resolved using a Cartesian grid size resolution of $33 \times 33 \times 33$ points and the representative r–z projections of pathlines of the cloth pieces' center of mass inside the washtub as shown with the red lines. (For interpretation of the references to color in this figure legend, the reader is referred to the web version of this article.)

Table 4
Operating conditions, physical and numerical parameters in the 3-D simulations.

Agitator peak rotation speed (ω_{max})[a]	120 rpm
Agitator rotational frequency (f)[a]	$2/\pi$ Hz
Cloth extensional stiffness (K_e)	8×10^5 N/m
Cloth in-plane shear stiffness (K_s)	3×10^2 N/m
Cloth bending stiffness (K_b)	1×10^{-5} N.m
Cloth torsional stiffness (K_t)	1×10^{-5} N.m
Cloth excess mass density ($\rho_s q$)[b]	9.3×10^{-2} kg/m^2
Cloth size ($L \times L$)	15 cm × 15 cm (square)
Average cloth thickness (q)	2.4×10^{-4} m
Water density (ρ_f)	1×10^3 kg/m^3
Water dynamic viscosity (μ)	10^{-1}–10^1 kg/(m s)
Dirac delta function half width (ε)	$2h_{\text{lateral}}$ and $2h_{\text{vertical}}$
Minimum Lagrangian to Eulerian mesh size ratio	1.15
$h_{\text{lateral}}/h_{\text{vertical}}$	3

[a] The agitator makes one full revolution before reversing.
[b] With respect to the mass of the displaced water (would be zero if neutrally buoyant in water).

and $h/r_o = 4.7 \times 10^{-2}$ has dropped to a 5% difference between $h/r_o = 4.7 \times 10^{-2}$ and $h/r_o = 3.5 \times 10^{-2}$. Additionally, note the significant decrease in the ratio of the standard deviation to the mean stresses for Re = 1200. Moreover, for the Re = 12,000 case

Table 6
Effect of grid resolution on the torque on the outer wall between the fourth and the twelfth agitation cycles for 16 cloth pieces with $\Delta t\omega_{max} = 5.0 \times 10^{-4}$. For * see the text.

h_{lateral}/r_o	Rms torque on the outer wall/τ_o		
	Re = 12,000	Re = 1200	Re = 120
7.0×10^{-2}	–*	5.85×10^{-4}	1.05×10^{-2}
4.7×10^{-2}	–*	5.39×10^{-4}	7.76×10^{-3}
3.5×10^{-2}	1.51×10^{-4}	5.36×10^{-4}	6.70×10^{-3}

Table 7
Effect of changing the time step on $|\bar{S}_{vM}|_{max}$ between the fourth and twelfth agitation cycles for 16 cloth pieces with Re = 1200, $h/r_o = 7.0 \times 10^{-2}$.

$\Delta t\omega_{max}$	$\lvert\bar{S}_{vM}\rvert_{max}/\sigma_o$	Standard deviation
$5.0 \times 10^{-4} \times 2$	11.86	7.44
5.0×10^{-4}	12.89	8.39
$5.0 \times 10^{-4}/2$	11.61	5.81

using $h/r_o = 7.0 \times 10^{-2}$ and 4.7×10^{-2}, some of the cloth pieces erroneously penetrated into the rotating agitator causing severe deformation of the cloth that distorted the statistics of the cloth stresses. This is the reason these values are not reported for those cases. These results show that the cloth stresses increase with Re, because with lower viscous forces, the fluid inertial forces dominate the cloth dynamics and result in more complex cloth mixing resulting in higher deformations (on the other hand with lower Re, the cloth motions are smoother and the cloth deformations are milder). Here, $|\bar{S}_{vM}|_{max}/\sigma_o$ is the ratio of the cloth elastic forces to the fluid inertial forces, and Table 5 suggests this ratio increases with Re, as the cloth motion gets more complex and the cloth deformations increase along with fluid inertial effects. However, the dimensionless torque in Table 6 show a decreasing trend with

Table 5
Effect of grid resolution on $|\bar{S}_{vM}|_{max}$ between the fourth and the twelfth agitation cycles for 16 cloth pieces with $\Delta t\omega_{max} = 5.0 \times 10^{-4}$. For * see the text.

h_{lateral}/r_o	$\lvert\bar{S}_{vM}\rvert_{max}/\sigma_o$			Standard deviation		
	Re = 12,000	Re = 1200	Re = 120	Re = 12,000	Re = 1200	Re = 120
7.0×10^{-2}	–*	12.89	6.20	–*	8.39	1.63
4.7×10^{-2}	–*	8.63	6.21	–*	4.01	1.65
3.5×10^{-2}	20.9	8.19	6.81	12.7	2.06	1.47

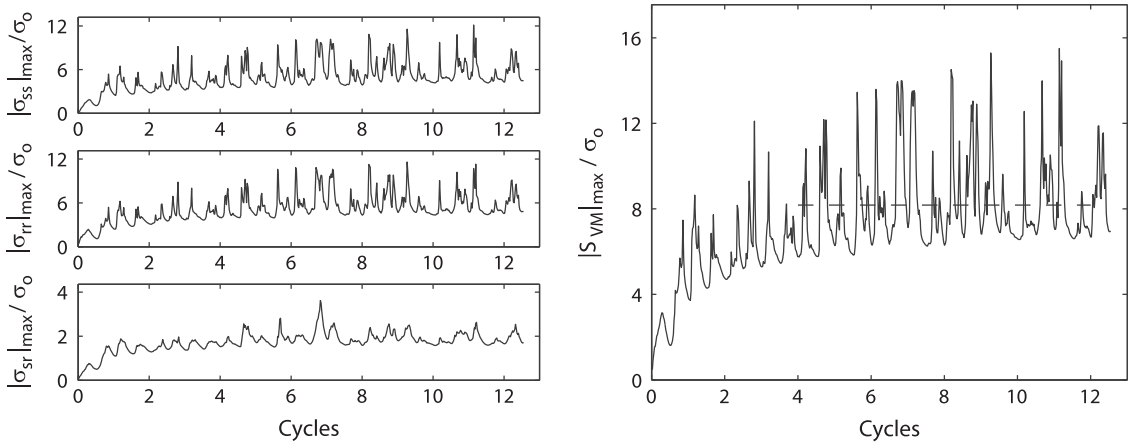

Fig. 6. The time histories of the maximum average cloth stresses $|\sigma_{ss}|_{max}$, $|\sigma_{rr}|_{max}$, $|\sigma_{sr}|_{max}$ (plots on the left); $|S_{VM}|_{max}$ (plot on the right) for 16 cloth pieces with Re = 1200, $\Delta t\omega_{max} = 5.0 \times 10^{-4}$. The dashed horizontal line on the right figure is the measured average of the von Mises stresses between the fourth and the twelfth agitation cycles.

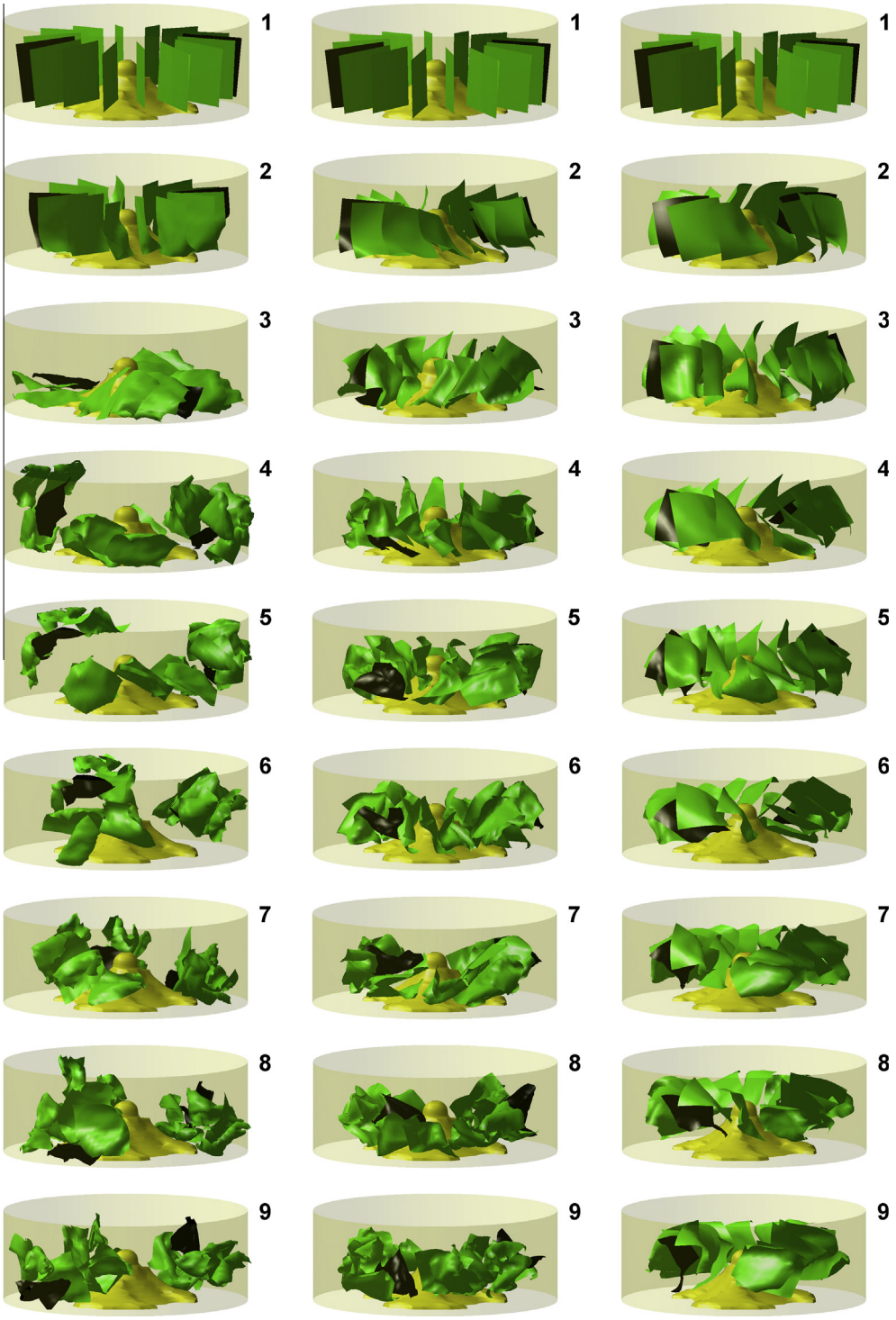

Fig. 7. Snapshots of the 16 cloth motion with Re = 12,000 (left column), 1200 (middle column), and 120 (right column), using the finest grid ($h/r_o = 3.5 \times 10^{-2}$). Snapshots differ by a half agitation cycle, corresponding to the full rotation of the agitator in one direction.

increasing Re. This is because this torque is more dependent on the skin friction (not the complexity of the motion within the wash basket); here the dimensionless skin friction is defined by $(\mu \partial u_t/\partial \mathbf{n})/(1/2\rho_f {\omega_{max}}^2 {r_o}^2)$, where u_t is the tangential velocity near the solid surface and $\mathbf{n}$ is the normal direction into the fluid. Sample time histories of the cloth stresses for 16 cloth pieces with Re = 1200, $\Delta t \omega_{max} = 5.0 = 10^{-4}$ are shown in Fig. 6.

Table 7 shows the effect of the time-step on the cloth stress magnitudes between the fourth and twelfth agitation cycles, for 16 cloth pieces, Re = 1200, and for a grid resolution of $h/r_o = 7.0 \times 10^{-2}$. These results show that for these conditions, the average cloth stresses fluctuate between 11.6 and 12.9, while the standard deviation fluctuates between 5.8 and 8.4. This time-step convergence study was performed at the coarse grid because: (i) the computational cost of further refining the time-step on fine grids was high and (ii) using large-time steps on finer grids occasionally led to simulation-failure when one of the cloth pieces came too close to the agitator and suffered very large deformations

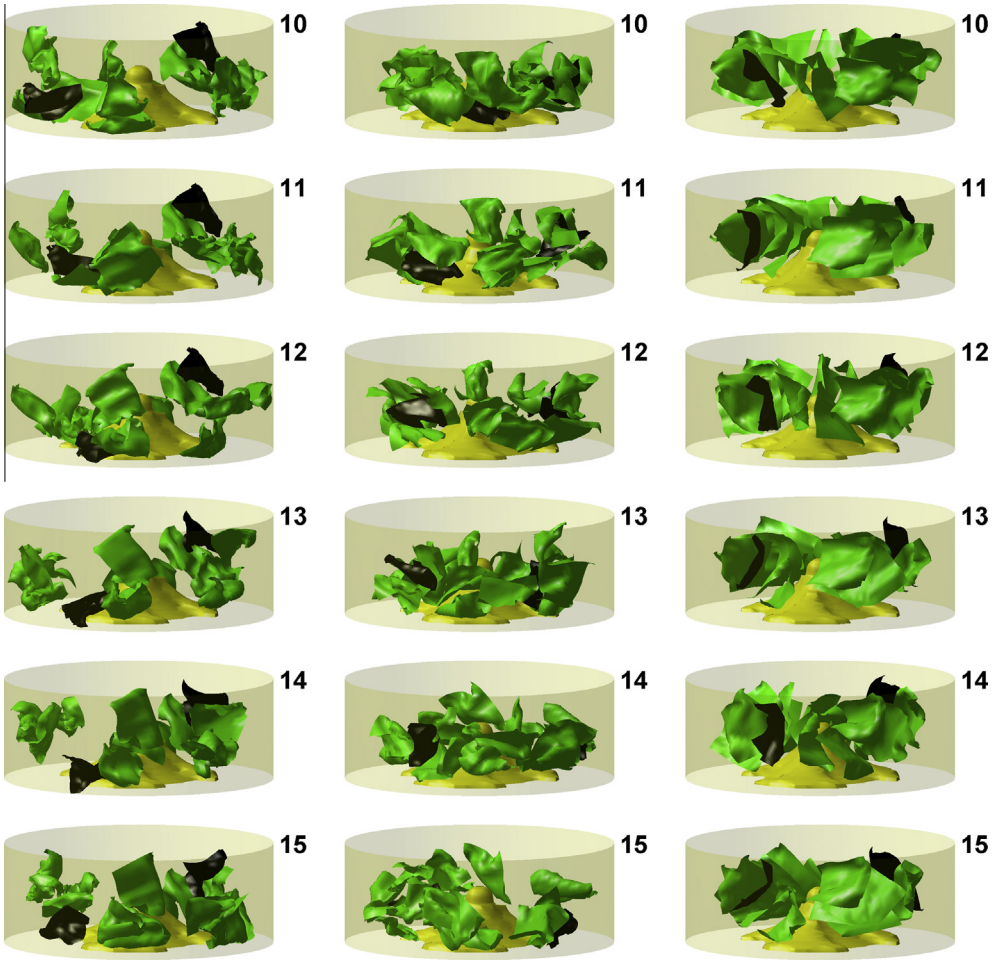

Fig. 7 (*continued*)

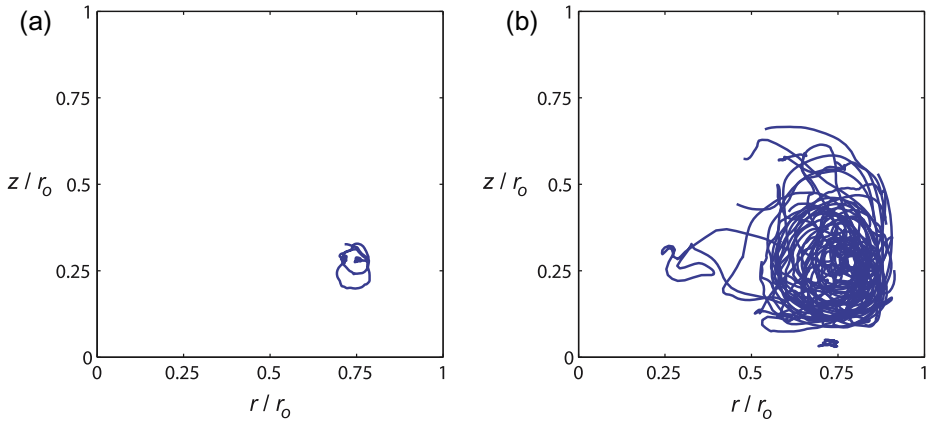

Fig. 8. All the cloth pieces' (left) and each cloth piece's (right) center of mass trajectories from the 4th to 12th agitation cycles at Re = 12,000.

at high speed – this will be further explained below. Table 7 confirms the results in Table 5 are relatively insensitive to time-step.

Representative pathlines of the cloth pieces' centers of mass inside the washtub are shown schematically in Fig. 5. For $Re \geqslant 1200$, the inertial effect of the agitator pushes the cloth pieces towards the outer drum along the bottom of the washtub as shown schematically in Fig. 5. Mass continuity requires these cloth pieces to elevate near the outer drum and then to move towards the center of the washtub, near the free surface. Finally, the cloth pieces descend near the center of the washtub. For coarse time-step or grid resolution, the simulations may fail if cloth pieces erroneously penetrate the agitator, since the agitator moves quickly compared to the surrounding fluid, which in turn leads to very high cloth elastic forces. On the other hand, at the lower Reynolds number (Re = 120), the cloth pieces mainly rotate about their relatively stationary center of mass.

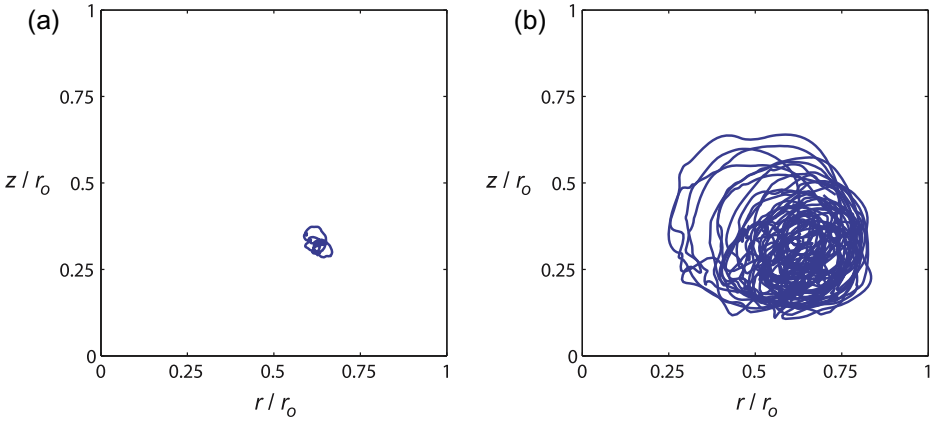

Fig. 9. All the cloth pieces' (left) and each cloth piece's (right) center of mass trajectories from the 4th to 12th agitation cycles at Re = 1200.

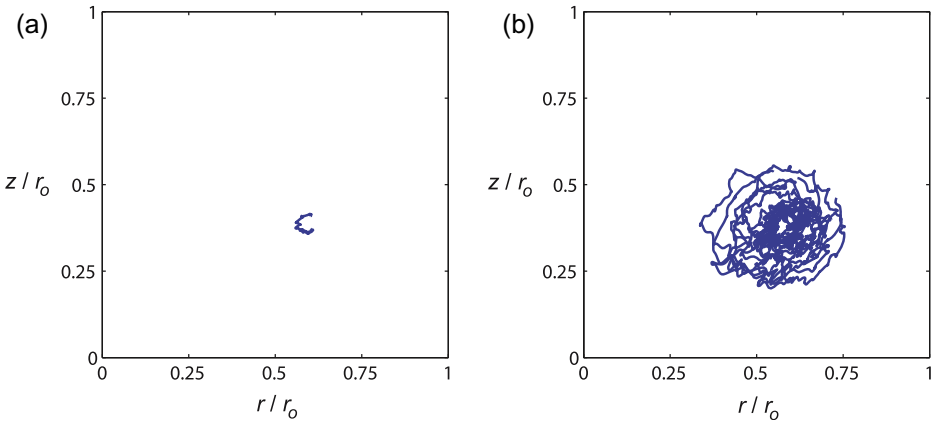

Fig. 10. All the cloth pieces' (left) and each cloth piece's (right) center of mass trajectories from the 4th to 12th agitation cycles at Re = 120.

Fig. 7 shows snapshots of the cloth motion for Re = 12,000 (left column), Re = 1200 (middle column), and Re = 120 (right column), using the finest grid ($h/r_o = 3.5 \times 10^{-2}$). The snapshots differ by a half agitation cycle, corresponding to a full rotation of the agitator in one direction. Simulation videos for $h/r_o = 3.5 \times 10^{-2}$ are attached as supplemental files to this paper.

The serial snapshots in Fig. 7 (and the videos) show that with lower Re, the tumbling rate is slower and the cloth pieces follow a more pronounced rotational motion with the agitator. In addition, Figs. 8–10 illustrate the trajectories of: (i) all the cloth pieces' common center of mass position and (ii) each of the 16 cloth pieces' center of mass position on a plane spanned by the height z from the bottom of the washtub and the horizontal radius $r = \sqrt{x^2 + y^2}$. This horizontal radius measures the cloth center of mass from the radial center of the agitator (Fig. 4).

The center of mass analyses of the cloth pieces in Figs. 8–10 conform to the trajectories plotted in Fig. 5 – especially for the cases with Re $\geqslant$ 1200. Further analyses of the cloth motion revealed that the azimuthal angular motion was only significant for the case with Re = 120. Note in Fig. 8 that for the case with Re = 12,000, one of the cloth pieces became stuck at the bottom, because it got too close to the rotating impeller at the bottom of the wash basket and then could not separate from it (this particular simulation is not used for the convergence arguments of Tables 5 and 6). This problem is caused by coarse grid resolution for Re = 12,000 and the assumption in the numerical method that the fluid velocity and the cloth velocity are locally the same. To better assess the effect of Re on the cloth scatter, Fig. 11 plots the rms distance of all the cloth points from their geometrically and time averaged centers from the plots in Fig. 8–10. Fig. 11 shows the range of scatter increases as the Re increases. However, the increase in the range of scatter is relatively modest between Re = 1200 and Re = 12,000, in comparison to the difference between Re = 120 and Re = 1200.

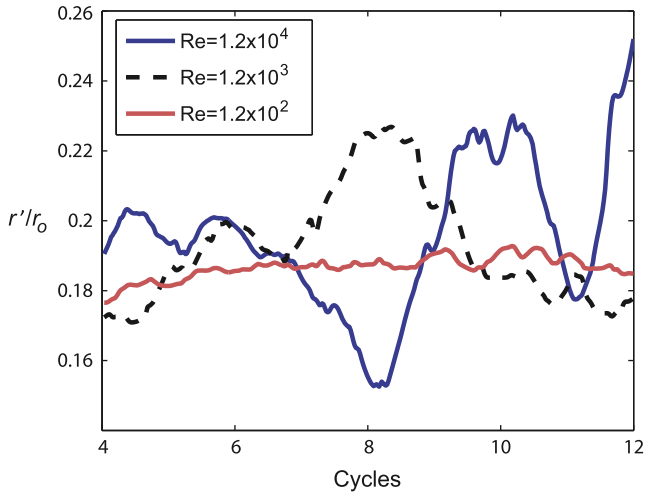

Fig. 11. The rms distance of all the cloth points (r') from their time and space average of the center of mass.

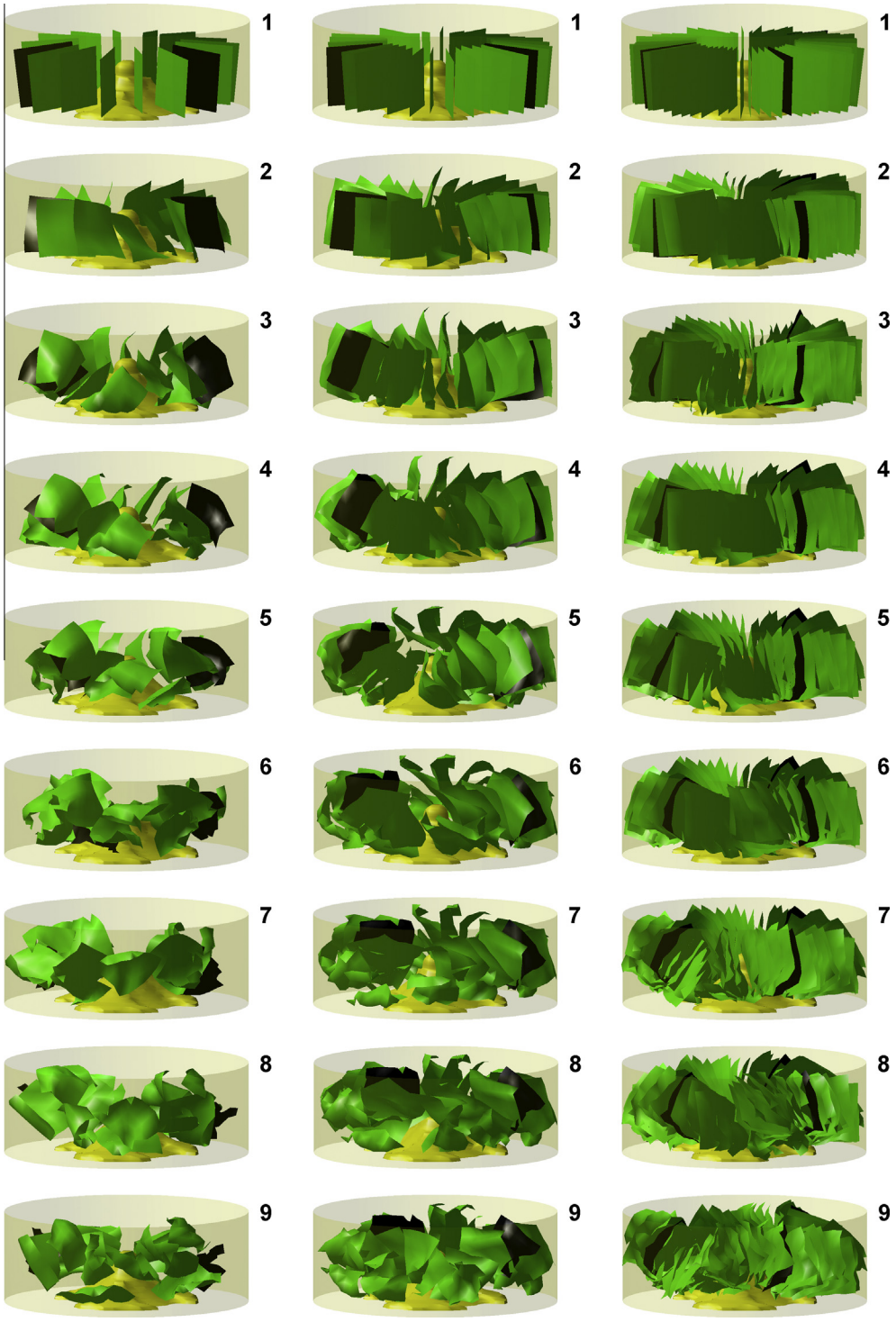

Fig. 12. Illustrative snapshots of the motion of 16 (left column), 32 (middle column), and 64 (right column) cloth pieces with Re = 1200, $\Delta t\omega_{max} = 5.0 \times 10^{-4}$, and $h_{\text{lateral}}/r_o = 7 \times 10^{-2}$. Snapshots differ by a half agitation cycle, corresponding to the full rotation of the agitator in one direction.

The effect of changing the cloth loading in the washtub is shown at Re = 1200 (approximately 1/1000th of a typical wash cycle Re) and $\Delta t\omega_{max} = 5.0 \times 10^{-4}$. The ratio of the total dry mass of the cloth pieces to the mass of the water in the washtub is approximately 1.7×10^{-3}, 3.3×10^{-3}, and 6.6×10^{-3} for the simulations with 16, 32, and 64 cloth pieces, respectively. The left, middle, and right columns of Fig. 12, respectively, show snapshots from the motion of 16, 32 and 64 cloth pieces. Again, the snapshots differ by a half agitation cycle, corresponding to a full rotation of the agitator in one direction. These simulations use $h_{\text{lateral}}/r_o = 7 \times 10^{-2}$.

From the simulation sequences in Fig. 12, the cloth pieces seem to move together (lack relative motion) when cloth loading is increased with fixed grid resolution. Although this is partly because the increased viscous effects due to the smaller inter-cloth spacing with heavier cloth loadings, the effect of overlapping regularized delta functions also causes the simulated cloth to closely follow its neighbors.

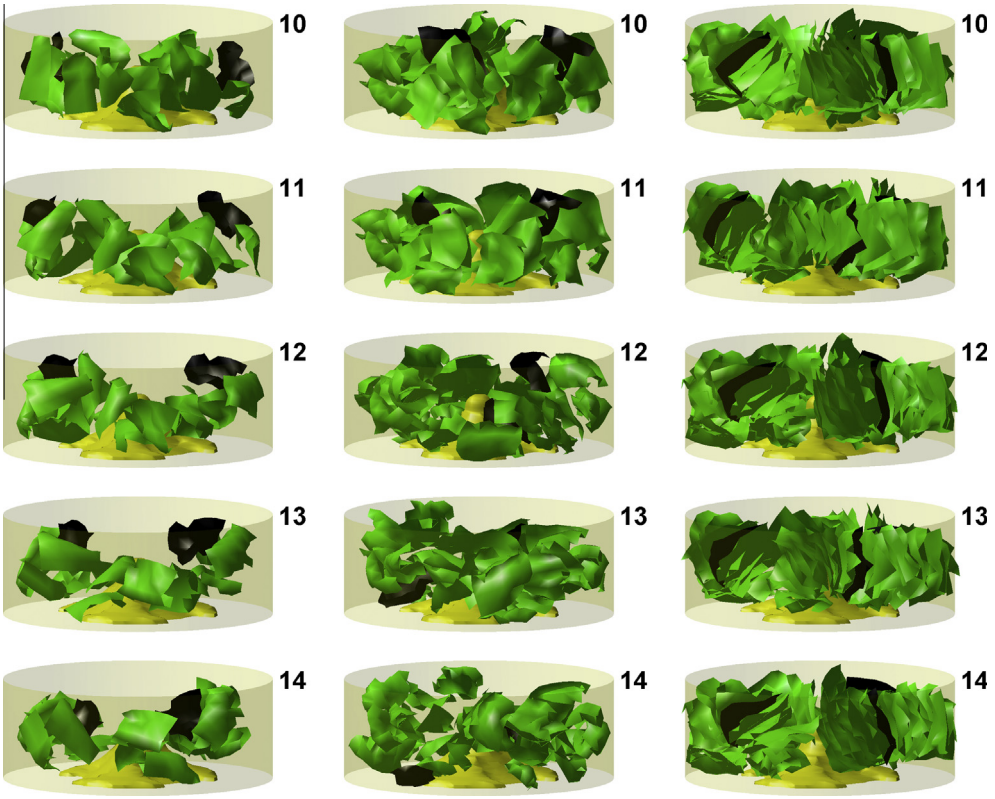

Fig. 12 (*continued*)

7. Conclusions

Two- and three-dimensional cloth/water washing machine simulations have been developed, and initial parametric studies have been conducted to assess the numerical technique, predicted cloth motion, and predicted cloth stresses. Here, the simulated motions of the cloth and water are both based on numerical solutions of the governing conservation laws for mass and momentum under excitation from a complex-shape agitator. The Navier–Stokes equations are used for the fluid. The equations for thin elastic plates undergoing arbitrary deformation are used for the cloth. The two solutions are coupled through an immersed boundary method that spreads the physical properties of the cloth onto the fluid-solution grid. The driving motions of the complex-shape agitator are similarly spread onto the fluid solution grid using a sharp level-set method to implement moving- and stationary-boundary conditions.

Although limited computational resources meant the simulation Reynolds number was kept artificially low compared that in actual clothes washing machines, the overall effort is successful. This contention is based on the following two observations. (1) The simulations capture the expected cloth tumbling motion in a vertical-axis washing machine. (2) The statistics of the cloth stresses and the torque exerted on the wash basket converged with mesh refinement.

These simulations were developed to predict cloth motion during a deep-water vertical-axis wash cycle. They show that when the Reynolds number is sufficiently high ($\mathrm{Re} \geqslant 1000$), the cloth pieces' center of mass (cm) positions move along the orbits shown in Fig. 5, but for lower Re the cloth pieces have a near constant center-of-mass position and merely rotate about their center of mass. Additionally, the cloth stresses were observed to increase and the torque exerted on the outer wash basket was observed to decrease with increasing Re. The variation of the center of mass positions of the cloth pieces are shown to increase with Re. However, the numerical method coupling the fluid and cloth leads to artificially stickiness between cloth pieces at high cloth loadings. Overall, the simulations look promising. Greater computational resources would better handle higher Re and allow the effects of different agitator motions to be assessed.

Acknowledgement

The authors gratefully acknowledge the support of the Whirlpool Corporation.

Appendix A. Derivation of F(η, *t*)

The following derivation of $\mathbf{F}(\boldsymbol{\eta}, t)$ is given in greater detail in Ref. [22] and it follows the classic theory of Ref. [12] for thin elastic plates. The unit vectors on the deformed cloth mid-plane (Fig. 1) are defined as

$$\mathbf{e}_s = \frac{\partial \mathbf{X}}{\partial s} \Big/ \left|\frac{\partial \mathbf{X}}{\partial s}\right|, \quad \mathbf{e}_r = \frac{\partial \mathbf{X}}{\partial r} \Big/ \left|\frac{\partial \mathbf{X}}{\partial r}\right|, \quad \text{and } \mathbf{e}_n = \frac{\mathbf{e}_s \times \mathbf{e}_r}{|\mathbf{e}_s \times \mathbf{e}_r|}. \tag{A.1, A.2, A.3}$$

The local area element of the plate's deformed mid-plane is

$$dA = |\mathbf{e}_s \times \mathbf{e}_r| ds dr = K ds dr \tag{A.4}$$

and the normal curvatures along constant-r and -s curves are, respectively,

$$\kappa_s = \left(\frac{\partial \mathbf{e}_s}{\partial s} \cdot \mathbf{e}_n\right) \Big/ \left|\frac{\partial \mathbf{X}}{\partial s}\right|, \quad \text{and } \kappa_r = \left(\frac{\partial \mathbf{e}_r}{\partial r} \cdot \mathbf{e}_n\right) \Big/ \left|\frac{\partial \mathbf{X}}{\partial r}\right|. \tag{A.5}$$

The geodesic torsion of the cloth deformed mid-plane is proportional to the τ that is defined here as

$$\tau = \frac{\partial^2 \mathbf{X}}{\partial r \partial s} \cdot \mathbf{e}_n. \tag{A.6}$$

Using these geometrical quantities and assuming a linear-elastic thin plate response, the following stress-($\mathbf{N}$) and internal moment-($\mathbf{M}$) resultants, across the cloth thickness q, can be found for an isotropic plate under plane-stress loading [22]

$$\begin{aligned} N_{ss} &= \frac{Eq}{1-\nu^2}\frac{1}{2}\left[\left(\frac{\partial \mathbf{X}}{\partial s}\cdot\frac{\partial \mathbf{X}}{\partial s}-1\right)+\nu\left(\frac{\partial \mathbf{X}}{\partial r}\cdot\frac{\partial \mathbf{X}}{\partial r}-1\right)\right], \\ N_{sr} &= N_{rs} = \frac{Eq}{1+\nu}\frac{1}{2}\left(\frac{\partial \mathbf{X}}{\partial s}\cdot\frac{\partial \mathbf{X}}{\partial r}\right), \\ N_{rr} &= \frac{Eq}{1-\nu^2}\frac{1}{2}\left[\left(\frac{\partial \mathbf{X}}{\partial r}\cdot\frac{\partial \mathbf{X}}{\partial r}-1\right)+\nu\left(\frac{\partial \mathbf{X}}{\partial s}\cdot\frac{\partial \mathbf{X}}{\partial s}-1\right)\right], \end{aligned} \tag{A.7}$$

$$\begin{aligned} M_{ss} &= -\tfrac{Eq^3}{12(1-\nu^2)}(\kappa_s+\nu\kappa_r), \\ M_{sr} &= -M_{rs} = \tfrac{Eq^3}{12(1+\nu)}\left(\tau/\left|\tfrac{\partial \mathbf{X}}{\partial s}\right|\left|\tfrac{\partial \mathbf{X}}{\partial r}\right|\right), \\ M_{rr} &= \tfrac{Eq^3}{12(1-\nu^2)}(\kappa_r+\nu\kappa_s), \end{aligned} \tag{A.8}$$

where E and ν are the Young's modulus and Poisson's ratio of the plate material. N_{sr} denotes to the stress-resultant along the r direction, but on a cloth section normal to s. M_{sr} is the internal moment-resultant due to N_{sr}. The total internal-moment resultants on the constant r and s lines, respectively, are defined in Eq. (A.9).

$$\begin{aligned} \mathbf{M}_s &= M_{ss}\mathbf{e}_r + M_{sr}\mathbf{e}_s \\ \mathbf{M}_r &= M_{rs}\mathbf{e}_r + M_{rr}\mathbf{e}_s \end{aligned}, \tag{A.9}$$

The flexible plate's stress- and moment-resultants lead to (Ref. [22]) the following force field (divergence of the stress-resultants), which is imposed as a body force in the fluid dynamic equations given in Sections 2 and 3:

$$\begin{aligned} \mathbf{F} = \frac{1}{K}\frac{\partial}{\partial s}\left(Q_1\mathbf{e}_n\left|\frac{\partial \mathbf{X}}{\partial r}\right| + N_{ss}\frac{\partial \mathbf{X}}{\partial s} + N_{sr}\frac{\partial \mathbf{X}}{\partial r}\right) + \frac{1}{K} \\ \times \frac{\partial}{\partial r}\left(Q_2\mathbf{e}_n\left|\frac{\partial \mathbf{X}}{\partial s}\right| + N_{rs}\frac{\partial \mathbf{X}}{\partial s} + N_{rr}\frac{\partial \mathbf{X}}{\partial r}\right), \end{aligned} \tag{A.10}$$

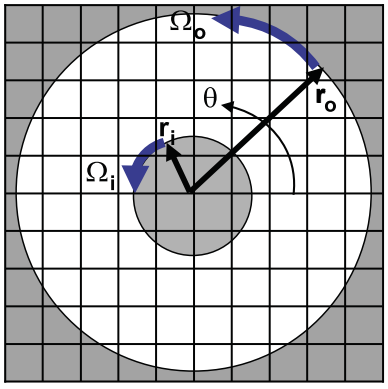

Fig. A.1. 2-D circular-Couette flow with a Cartesian grid.

where Q_1 and Q_2 are the shear forces due to the bending moments that are obtained from the angular momentum equation given in Eq. (A.11)), without the inertial effects (see [22] for a discussion on this assumption).

$$\frac{\partial}{\partial s}\left(\mathbf{M}_s\left|\frac{\partial \mathbf{X}}{\partial r}\right|\right) + \frac{\partial}{\partial r}\left(\mathbf{M}_r\left|\frac{\partial \mathbf{X}}{\partial s}\right|\right) + \left|\frac{\partial \mathbf{X}}{\partial s}\right|\left|\frac{\partial \mathbf{X}}{\partial r}\right|(-Q_1\mathbf{e}_r + Q_2\mathbf{e}_s) = 0. \tag{A.11}$$

Appendix B

The fluid-rigid solid interaction part of the simulation was validated by solving the 2-D laminar circular-Couette flow, as well as the external flow over a cylinder at Re = 100.

The geometry of the first problem is as given in Fig. A.1. There is an inner cylinder with a radius r_i that is moving with an angular speed Ω_i and there is an outer cylinder with a radius r_o that is moving with an angular speed Ω_o. The space between the inner and outer cylinders is assumed to be filled with an incompressible Newtonian fluid. The exact solution of this problem is given by:

$$\mathbf{u_{ex}} = \left[\left(\frac{\Omega_i r_i^2 - \Omega_o r_o^2}{r_i^2 - r_o^2}\right)r + \left(\frac{r_i^2 r_o^2}{r_i^2 - r_o^2}\right)\frac{\Omega_o - \Omega_i}{r}\right]\mathbf{e}_\theta \tag{A.12}$$

where $\mathbf{e_\theta}$ is a unit vector rotating along θ shown in Fig. A.1.

For laminar and steady flow solutions, the convective and pressure terms of the Navier–Stokes equations drop out in the exact solution. For $\Omega_i/\Omega_o = 6.13$, $r_i/r_o = 0.34$, $\mathrm{Re} = \rho_f r_o \Omega_o (r_o - r_i)/\mu = 131$, and $\Delta t r_o \Omega_o/(r_o - r_i) = 2.5 \times 10^{-3}$, Tables A.1 and A.2 compare the simulation and analytical results using a sharp Heaviside function (H) In Eq. (9) and regularized Heaviside function with $\gamma = 2h$, respectively, where the maximum and root-mean-square (rms) error are defined in Eq. (A.13). In Eq. (A.13) $\mathbf{u}_{\mathrm{sim}}$ is the numerically predicted velocity and $\mathbf{u}_{ex}$ is the exact solution from Eq. (A.12).

$$\begin{aligned} &\text{Maximum error}: \max\left(\frac{\mathbf{u}_{\mathrm{sim}} - \mathbf{u}_{\mathrm{ex}}}{\mathbf{u}_{\mathrm{ex}}}\right), \\ &\text{Rms error}: \left[\frac{1}{N_{\mathrm{grid}}}\sum_{N_{\mathrm{grid}}}\left(\frac{\mathbf{u}_{\mathrm{sim}} - \mathbf{u}_{\mathrm{ex}}}{\mathbf{u}_{\mathrm{ex}}}\right)^2\right]^{1/2} \end{aligned} \tag{A.13}$$

Tables A.1 and A.2 show that the convergence rate of the formulation given in Eqs. (9) and (10) are higher by using regularized Heaviside functions (H) with $\gamma = 2h$; however, the errors on the coarse grid sizes were lower with using the sharp Heaviside functions. This latter observation is the reason for why the current simulation uses the sharp Heaviside formulation in the washing machine simulations that have coarse grid resolutions, especially for the 3-D case.

In a second validation case, the fluid-rigid solid interaction part of the simulation was used to predict the maximum and minimum lift coefficient (C_L), and mean drag coefficient ($\overline{C}_D$) induced on a circular cylinder in an external flow (Fig. A.2), as well as the Strouhal number (St) corresponding to the non-dimensional frequency of the vorticity shedding; these numbers are defined as:

$$C_D = \frac{F_x}{\frac{1}{2}\rho_f U_o^2 D}, \quad C_D = \frac{F_y}{\frac{1}{2}\rho_f U_o^2 D}, \quad \mathrm{St} = \frac{fD}{U_o},$$

Table A.1
Effect of the grid resolution on the accuracy of the 2-D steady, laminar, and circular Couette flow with a sharp H.

h/r_i	Maximum error	Convergence Rate	Rms error	Convergence rate
0.0646	0.0365	–	0.0105	–
0.0324	0.0309	0.24	7.95×10^{-3}	0.40
0.0162	0.012	1.4	3.47×10^{-3}	1.2

Table A.2
Effect of the grid resolution on the accuracy of the 2-D steady, laminar, and circular Couette flow with a regularized H.

h/r_i	Maximum error	Convergence rate	Rms error	Convergence rate
0.0646	0.1133	–	0.0469	–
0.0324	0.04	1.5	0.0167	1.5
0.0162	0.01	2.0	4.0×10^{-3}	2.1

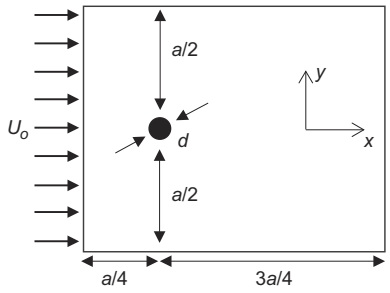

Fig. A.2. Numerical setup of the simulations of a 2D flow past a circular cylinder.

Table A.3
Comparison of the present results with the others in the literature at Re = 100.

	$\overline{C}_D$	C_L	St	Domain size
Present ($\gamma = 0$)	1.40	±0.33	0.166 ± 0.0098	$30d \times 30d$
Present ($\gamma = 0$)	1.34	±0.33	0.166 ± 0.0098	$60d \times 60d$
Present ($\gamma = 2h$)[a]	1.43	±0.37	0.166 ± 0.0098	$30d \times 30d$
Present ($\gamma = 2h$)[a]	1.41	±0.37	0.166 ± 0.0098	$60d \times 60d$
Ref. [32]	–	–	0.163	Experiment
Ref. [31]	1.33	±0.32	0.165	$70d \times 100d$
Ref. [33]	1.39	–	0.16	$30d \times 15d$
Ref. [34]	1.42	0.29 (rms)	0.164	$32d \times 16d$
Ref. [35]	1.37	±0.323	0.160	$30d \times 15d$
Ref. [36]	1.40	±0.34	0.168	$29.9d \times 16.7d$

[a] Note that, the results with $\gamma = 2h$ presented here were yet to converge with respect to the grid size (a grid size of 1025×1025 was used for a domain size of $60d \times 60d$ and a grid size of 2049×2049 was used for a domain size of $30d \times 30d$), but the results presented here with sharp H are converged.

where F_x and F_y are the fluid-forces induced on the cylinder on the horizontal (positive: downstream direction) and vertical (positive: upward direction), U_o is the inflow speed, and f is the frequency of the vorticity shedding (as measured from the fluctuations of the F_x and F_y). In the simulations the boundary conditions were specified as inflow at the upstream, a convective boundary condition, $\frac{\partial \mathbf{u}}{\partial t} + c_e \frac{\partial \mathbf{u}}{\partial x} = \mathbf{0}$, at the downstream boundary, where c_e is the average horizontal speed (u) at the downstream, as suggested by [31], and at the top and bottom boundaries: (i) similar convective boundary conditions for the vertical component of the flow speed (v) and (ii) a condition on u such that the viscous stresses are continuous at the top and bottom boundaries. Note that this validation study also tests the convective, pressure, and unsteady flow effects that were missing in the previous steady Couette flow study.

The results for $\mathrm{Re} = \rho_f U_o D/\mu = 100$ are given in Table A.3 with a few other results from the published literature. The results show that the predictions with the current simulation using $\gamma = 0$ (sharp H) in Eq. (9) and with a domain size of ($60d \times 60d$) yield to comparative results with respect to the other existing results. On the other hand, the simulation predictions using a regularized H with $\gamma = 2h$ yielded into slightly higher lift and drag forces than the ones given in the literature.

Appendix C. Supplementary material

Supplementary data associated with this article can be found, in the online version, at http://dx.doi.org/10.1016/j.compfluid.2014.05.005.

References

[1] Ward D. Modeling of a horizontal-axis domestic washing machine. J Text Inst, Part 1, Fiber Sci Text Technol 2000;91:207–34.
[2] Boyraz P, Gunduz M. Dynamic modeling of a horizontal washing machine and optimization of vibration characteristic using genetic algorithms. Mechatronics 2013;23:581–93.
[3] Bascetta L, Rocco P, Zanchettin AM, Magnani G. Velocity control of a washing machine: a mechatronics approach. Mechatronics 2012;22:778–87.
[4] Lim H-T, Jeong W-B, Kim K-J. Dynamic modeling and analysis of drum-type washing machine. Int J Precis Eng Manuf 2010;11(3):407–17.
[5] Lu J, Zheng C. Dynamic cloth simulation by isogeometric analysis. Comput Methods Appl Mech Eng 2014;268:475–93.
[6] Bridson R, Fedkiw R, Anderson J. Robust treatment collisions, of contact and friction for cloth animation. In: SIGGRAPH '02 Proceedings of the 29th annual conference on computer graphics and interactive techniques. New York, NY, USA: ACM; 2002. p. 594–603. http://dx.doi.org/10.1145/566570.566623.
[7] Baraff D, Witkin A. Large steps in cloth simulation. In: SIGGRAPH '98 Proceedings of the 25th annual conference on computer graphics and interactive techniques. New York, USA: ACM; 1998. p. 43–54. http://dx.doi.org/10.1145/280814.280821.
[8] Zhao YF, Wong TN, Tan ST, Chen WJ. A model for simulating flexible surfaces of cloth objects. Comput Struct 1997;63(1):133–47.
[9] House DH, DeVaul RW, Breen DE. Towards simulating cloth dynamics using interacting particles. Int J Clothing Sci Technol 1996;8(3):75–94.
[10] Chen B, Govindaraj M. A physically based model of fabric drape using flexible shell theory. Text Res J 1995;65(6):324–30.
[11] Terzopoulos D, Platt J, Barr A, Fleischer K. Elastically deformable models. SIGGRAPH '87 Proceedings of the 14th annual conference on computer graphics and interactive techniques. New York, USA: ACM; 1987. p. 205–14. http://dx.doi.org/10.1145/37401.37427.
[12] Love AEH. A treatise on the mathematical theory of elasticity. 4th ed. Dover Publications; 1944.
[13] Brown DL, Cortez R, Minion ML. Accurate projection methods for the incompressible Navier–Stokes equations. J Comput Phys 2001;168(2):464–99.
[14] Peskin CS. Flow patterns around heart valves – a numerical method. J Comput Phys 1972;10(2):252–71.
[15] Akcabay DT, Young YL. Hydroelastic response and energy harvesting potential of flexible piezoelectric beams in viscous flow. Phys Fluids 2012;24:054106.
[16] Zhu L, He G, Wang S, Miller L, Zhang X, You Q, et al. An immersed boundary method based on the lattice Boltzmann approach in three dimensions, with application. Comput Math Appl 2011;61:3506–18.
[17] Zhu L. Simulation of elastic filaments interacting with a viscous pulsatile flow. Comput Methods Appl Mech Eng 2008;197:2265–74.
[18] Zhu L. Simulation of an inhomogeneous elastic filament falling in a flowing viscous fluid. Phys Fluids 2007;19:017113.
[19] Dillon R, Fauci L, Fogelson A, Gaver D. Modeling biofilm processes using the immersed boundary method. J Comput Phys 1996;129:57–73.
[20] Fauci LJ, Mcdonald A. Sperm motility in the presence of boundaries. Bull Math Biol 1995;57:679–99.
[21] Fauci LJ, Peskin CS. A computational model of aquatic animal locomotion. J Comput Phys 1988;77:85–108.
[22] Akcabay DT. Physics based washing machine simulations. Ph.D. thesis, University of Michigan, Ann Arbor, MI, USA; 2007.
[23] Peskin CS. The immersed boundary method. Acta Numerica 2002:479–517.
[24] Leveque RJ, Li ZL. Immersed interface methods for Stokes flow with elastic boundaries or surface tension. SIAM J Sci Comput 1997;18(3):709–35.
[25] Lee L. Immersed interface methods for incompressible flow with moving interfaces. Ph.D. Thesis, University of Washington, Seattle, WA, USA; 2002.
[26] Lee L, Leveque RJ. An immersed interface method for incompressible Navier–Stokes equations. SIAM J Sci Comput 2003;25(3):832–56.
[27] Son G. A level set method for incompressible two-fluid flows with immersed solid boundaries. Numer Heat Transfer Part B-Fund 2005;47(5):473–89.
[28] Al-Rawahi N, Tryggvason G. Numerical simulation of dendritic solidification with convection: two-dimensional geometry. J Comput Phys 2002;180(2):471–96.
[29] Aref H. Stirring by chaotic advection. J Fluid Mech 1984;143:1–21.
[30] Teixeira J, Reynolds CA, Judd K. Time step sensitivity of nonlinear atmospheric models: numerical convergence, truncation error growth, and ensemble design. J Atmos Sci 2007;64(1):175–89.
[31] Kim J, Kim D, Choi H. An immersed-boundary finite-volume method for simulations of flow in complex geometries. J Comput Phys 2001;171(1):132–50.
[32] Williamson CHK. Vortex dynamics in the cylinder wake. Ann Rev Fluid Mech 1996;28:477–539.

[33] Silva ALFLE, Silveira-Neto A, Damasceno JJR. Numerical simulation of two-dimensional flows over a circular cylinder using the immersed boundary method. J Comput Phys 2003;189(2):351–70.
[34] Tseng YH, Ferziger JH. A ghost-cell immersed boundary method for flow in complex geometry. J Comput Phys 2003;192(2):593–623.
[35] Le DV, Khoo BC, Peraire J. An immersed interface method for viscous incompressible flows involving rigid and flexible boundaries. J Comput Phys 2006;220(1):109–38.
[36] Su SW, Lai MC, Lin CA. An immersed boundary technique for simulating complex flows with rigid boundary. Comput Fluids 2007;36(2):313–24.